Nuclear Instruments and Methods in Physics Research B 406 (2017) 15–24

Contents lists available at ScienceDirect

Nuclear Instruments and Methods in Physics Research B

journal homepage: www.elsevier.com/locate/nimb

Analytical possibilities of highly focused ion beams in biomedical field

M.Q. Ren [a,*], X Ji [b], S.K. Vajandar [a], Z.H. Mi [a], A. Hoi [c], T Walczyk [b], J.A. van Kan [a], A.A. Bettiol [a], F. Watt [a], T. Osipowicz [a]

[a] Centre for Ion Beam Applications, Department of Physics, National University of Singapore, Singapore
[b] Department of Chemistry, National University of Singapore, Singapore
[c] Bioprocessing Technology Institute, Centros Building, 20 Biopolis Way, Singapore 138668, Singapore

ARTICLE INFO

Article history:
Received 26 August 2016
Received in revised form 30 December 2016
Accepted 4 January 2017
Available online 18 January 2017

Keywords:
Focused ion beam
PIXE
RBS
STIM
Diseases
Whole cell imaging

ABSTRACT

At the Centre for Ion Beam Applications (CIBA), a 3.5 MV HVEE Singletron™ accelerator serves to provide MeV ion beams (mostly protons or He^+) to six state-of-the-art beam lines, four of which are equipped with Oxford triplet magnetic quadrupole lens systems. This facility is used for a wide range of research projects, many of which are in the field of biomedicine. Here we presented a discussion of currently ongoing biomedical work carried out using two beamlines:

(a) The Nuclear Microscopy (NM) beamline is mainly used for trace elemental quantitative mapping using a combination of Particle Induced X-ray Emission (PIXE), to measure the trace elemental concentration of inorganic elements, Rutherford Backscattering Spectrometry (RBS), to characterise the organic matrix, and Scanning Transmission Ion Microscopy (STIM) to provide information on the lateral areal density variations of the specimen. Typically, a 2.1 MeV proton beam, focused to 1–2 μm spot size with a current of 100 pA is used.
(b) The high resolution single cell imaging beamline is equipped with direct STIM to image the interior structure of single cells with proton and alpha particles of sub-50 nm beam spot sizes. Simultaneously, forward scattering transmission ion microscopy (FSTIM) is utilized to generate images with improved contrast of nanoparticles with higher atomic numbers, such as gold nanoparticles, and fluorescent nanoparticles can be imaged using Proton Induced Fluorescence (PIF). Lastly, in this facility, RBS has been included as an option if required to determine the depth distribution of nanoparticles in cells, albeit with reduced spatial resolution.

1. Introduction

The research work at CIBA largely depends on the use of ion beams with precisely controlled phase space characteristics, as delivered by a 3.5 MV Singletron (High Voltage Engineering Europa B.V., Netherlands), and the possibility to form highly focused nano-sized beam spots via quadrupole lens systems (Oxford Microbeams, UK). The Singletron produces high brightness light ion beams with a typical long term (~5 h) energy stability of a few tens of eV [1].

Here we discuss two beamlines involved in biomedical research applications, the Nuclear Microscopy line and the Single Cell Imaging line. These beamlines differ in the techniques employed.

The minimum beam-spot size that can be realized in a magnetic quadrupole lens system depends on the size of the object apertures, and these in turn will, for a given beam brightness, determine the available beam current on the sample. The Nuclear Microscopy beamline is optimized for analytical experiments, and for the analysis modes of PIXE and RBS, a beam current around 100 pA is required in order to be able to generate images within acceptable run times, typically 0.5–2 h. These conditions require an object aperture dimension of a few tens of micrometers, for which the minimum achievable beam-spot size is then around a third of a micrometer [2,3]. On the other hand, the Single Cell Imaging line employs techniques which do not involve such relatively high beam currents, and is optimized for techniques where the probability for an ion to be detected approaches unity. It is then possible to work with object apertures of a few microns, for which spot sizes of 20 nm have been achieved, for ion counts rates of around 10,000 ions per second. This allows techniques such as

* Corresponding author.
E-mail address: phyrenmq@nus.edu.sg (M.Q. Ren).

http://dx.doi.org/10.1016/j.nimb.2017.01.004
0168-583X/

direct STIM (on-axis STIM), FSTIM (forward off-axis STIM), PIF (proton induced fluorescence) and AIF (alpha induced fluorescence) to be carried out at nano-resolutions [4].

It was recognized a long time ago that MeV light ions traverse matter along well-defined straight paths, therefore they are unique probes for relatively thick (microns to tens of microns) tissue sections and single whole cells with good spatial resolutions, and at ppm detection limits [5].

2. Description of the nuclear microscope beam line

The CIBA nuclear microscope beamline [2,3] incorporates an Oxford Microbeams OM2000 end station and an OM50 target chamber with a 150 mm working distance between target and the OM50 quadrupole lens configured in the high excitation triplet mode. This beamline is equipped with an Oxford Microbeams OM50 target chamber (shown schematically in Fig. 1) which has eight ports: one for the beam pipe, one for a long working distance zoom optical microscope with a glass covered port for viewing the target and the other ports for fitting various detection systems such as PIXE, RBS, STIM, ERDA and ion induced fluorescence measurements with a photo multiplier tube (PMT). A Faraday cup is mounted together with STIM setup behind the sample for beam current measurement when the target is a thin biological specimen. For most of the measurements of biomedical samples carried out in this beamline, the target is tilted at an angle of 45° to the beam and to the PIXE detector positioned at 90° to the beam. The optical microscope is mounted at 45° to the beam (see Fig 1). This geometrical arrangement allows the PIXE detector to be positioned close to the target, which results in large PIXE detection solid angles, thereby maximising trace element detection. The RBS detector is mounted above the incoming beam, at a scattering angle of 160°. The STIM detector sits behind the sample on a vacuum sealed rotary shaft, and can be rotated between 0° and 20°, thereby facilitating both on-axis (direct) STIM or off-axis STIM measurements. For thin samples, a Faraday cup can be used to measure the beam charge via a vacuum feed-through and a charge digitiser module. All data acquisition functions are implemented via the OMDAQ 2007, a Windows 7 based DAQ system [6].

Biomedical applications typically involve the characterisation of tissue or cell specimens. In such studies, the Nuclear Microscopy beamline is typically operated with a 2.1 MeV proton beam and a beam spot size of 1–2 μm, at on-sample beam currents of 100–500 pA. The beam is scanned by a pre-lens magnetic scanning coil over a region up to 4 × 4 mm. The data acquisition system [6] allows the scanning of predefined areas as well as line scans. Furthermore, all experimental data and parameters can be saved in event by event list-mode files, so that off-line re-runs of the experiments is possible. This mode is advantageous for biomedical analyses, because biomedical specimen often have areas of interest which are not obvious before the experiment is carried out.

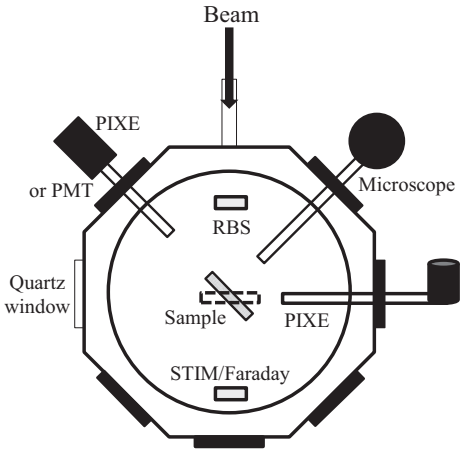

Fig. 1. Target chamber of nuclear microscopy beamline.

3. Description of the single cell imaging beam line

Recently, a Single Cell Imaging beam line [4] was set up at a position 30 degrees after the switcher magnet. This development was driven by the increasing interest in imaging techniques with resolutions substantially below the optical diffraction limit of 200 nm. Electron microscopy, which of course offers such resolutions, is however limited to surface analysis because the electron beams suffer large angle scattering as they pass through the sample. MeV light ions, in contrast, will travel with essentially straight trajectories [7] Therefore, to a good approximation, a finely focused MeV light ion beam will maintain its resolution as it traverses through a single whole biological cell. Using the Single Cell Imaging end station, we have demonstrated that it is possible to focus MeV proton beams to spot sizes well below 50 nm, and assemble STIM and PIF (proton induced fluorescence) images of whole cells, revealing interior structures (nuclei, organelles) of whole cells [8].

This single cell end station is mounted on an optical table, and incorporates a quadrupole lens system made up of 3 compact OM52 quadrupole lenses [9] operated in a triplet mode. An electrostatic scanning system is used to scan the beam over the target [10]. The target chamber has been constructed with in-built optical and fluorescent microscopes for sample imaging and for target positioning, and incorporates a highly stable sample stage driven by piezoelectric drivers allowing 25 mm movement in all the three spatial directions. Typically, an experiment is started by focussing the ion beam under optical control on a quartz target, and checking the resolution using a proton beam written free-standing nickel grid [11]. The focussing of beam spot sizes below 250 nm is usually done via STIM, using a Hamamatsu S1223 pin-diode or a conventional RBS detector and the Ni grid. An annular surface barrier detector is mounted at 180° scattering angle for quantitative measurements of high Z elements at ~300 nm resolution.

A Hamamatsu photomultiplier (model PMT R7401P) is used for ion induced fluorescence imaging. The data acquisition system used in this beam-line can generate up to 2048 × 2048 pixel imaging using the IonDAQ package [12].

The single cell imaging beam line is routinely operated at sub 100 nm resolution for imaging single cell specimen using techniques such as direct STIM using proton or alpha particles for cell interior structures, FSTIM for enhanced contrast for cells loaded with high Z elements such as gold nanoparticles, and proton and alpha induced fluorescence imaging as well as secondary electron imaging [13]. It is worth noting that alpha STIM gives much better contrast than proton STIM due to the higher energy loss of alpha particles in matter compared to that of protons. However, alpha particles often have much higher bleaching rates (quenching of optical emission) during fluorescence imaging compared to protons.

4. Biomedical applications of nuclear microscopy beam line

PIXE uses MeV protons to produce characteristic X-ray photons via inelastic Coulomb collisions. A large solid angle spectroscopy system is then used to measure the energies of X-rays, typically large surface area Si(Li) detectors are used. In recent years, these are increasingly being replaced by Silicon Drift Detector (SDD), which do not require LN_2 cooling. The energy of characteristic X-rays is unique to the parent atom, thus the identification of partic-

ular elements is possible. In order to extract quantitative trace elemental maps of thin biological tissue samples, a combination of PIXE and RBS is required: The RBS data is used to provide information on the thickness, the matrix composition and the areal density of the sample. In addition, the charge collected during a measurement can be determined. In many thin biological samples the accumulation of PIXE/RBS maps is rather slow, and so off-axis STIM is frequently used to acquire a map of the areal density of the sample using the energy loss information. Off-axis STIM thereby allows the positioning of region of interest within minutes. In CIBA, using the combination of PIXE, RBS and off-axis STIM at 2.1 MeV proton beam focused to 1–2 μm spot sizes, we have successfully carried out many studies in biomedicine, including a study of Parkinson's Disease [14], measuring the correlation of trace element iron content and the neuronal distribution in the substantia nigra region of the brain. Atherosclerosis studies [5,15] were also carried out to investigate the correlation between atherosclerotic lesion growth and the iron and zinc concentrations and we have also investigated elemental changes in the carotid artery of apolipoprotein E deficient mice under the influence of probucol [16]. The energy of proton beam is chosen to be 2.1 MeV in order to avoid a strong carbon nuclear elastic resonance close to 2 MeV which would otherwise distort the RBS spectra and hamper the data analysis.

In order to process the measured data, several highly specialized software packages are used: SIMNRA [17] is a code used to fit RBS data, i.e. to find a sample thickness and major element composition that will closely reproduce the measured spectra. From such simulations, the charge and the sample matrix thickness and composition are derived. The Gupixwin [18] package is used to extract quantitative information of the trace elements.

Below are two examples of the biological applications currently carried out in CIBA.

4.1. Flash frozen human carotid artery tissue sample analysis

The analysis of human carotid artery tissue was a collaboration between CIBA and the National University Hospital, Singapore, Division of Vascular and Endovascular Surgery, where we obtained human carotid artery samples for evaluation, especially the calcium and iron concentration distributions. This work was initiated because of an earlier finding that in rabbits with induced advanced atherosclerotic lesions, an anti-correlation between calcium and iron distributions was observed [19].

We have analyzed calcified advanced atherosclerotic lesions from the carotid artery of patients who suffered from an ischemic stroke. Limited amounts of tissue were collected during surgery and prepared using the standard procedure for Nuclear Microscopy tissue samples as given elsewhere [13]. Briefly, the tissue blocks were rinsed with de-ionized water to remove residual blood, embedded with Jung Tissue-Freezing Medium (Leica Instruments, Germany) and frozen immediately (ideally within minutes of surgery) in liquid nitrogen. The samples were transported on dry ice and stored at −80 °C until cryo-sectioning took place. It is advisable not to leave the fresh tissue blocks in any fixative solution, to avoid ionic redistribution in the tissue and ingress of impurities from the solution.

16 μm thick unfixed and unstained tissue slices were sectioned using a cryostat (Jung Frigocut 2800E, Leica, Nussloch, Germany) at chamber temperature of −23 °C and sample temperature of -18° C. The thin sections were picked up on pioloform wrapped aluminium nuclear microscope holders and freeze dried at −20 °C freezer. Adjacent sections were picked up on polylysine-coated glass slides (Polyscience, Inc., USA.) for H&E staining for morphology studies and to identify areas of interest selection before the NM scans. Elemental mapping of thin tissue sections was then carried out using the Nuclear Microscopy beam line.

A 2.1 MeV proton beam with a spot size of 1 μm was scanned over the freeze-dried tissue section. An area of $600 \times 600\ \mu m^2$ without any atherosclerotic lesion was scanned and used as a control. A typical off-axis STIM image is shown in Fig. 2b, which was obtained within five minutes. The image shows an areal density map of $600 \times 600\ \mu m$ artery area including the intima, media and adventitia (indicated in Fig. 2a). Table 1 presents the trace elemental concentrations measured in various regions of this lesion-free human arterial wall, as derived from the PIXE spectra. Fig. 3 displays the elemental concentration information in a bar graph.

The main purpose of this study was to scan and measure using Nuclear Microscopy the elemental profile in human carotid arteries with advanced atherosclerotic lesions. The advanced lesions are largely calcified and therefore rather brittle, and during cryosectioning they often broke into powdery fragments. The NM measurement results confirm that there is a large amount of calcium present in the human advanced lesion, as shown in Fig. 4, in which a distinct difference between carotid artery with advanced lesion and the control is clearly demonstrated.

The elemental Fe and Ca maps in Fig. 4 are in agreement with our earlier studies on rabbit aortic arteries exhibiting advanced atherosclerotic lesions [5], and also in carotid arteries of apolipoprotein E deficient mice [16]: These showed a consistent trend for atherosclerotic lesions, where higher iron concentration are observed, compared to the underlying arterial wall, and calcification in the interface between the atherosclerotic lesion and the artery wall is present. In addition, an inverse correlation between iron and calcium distributions found in our previous study [19] is also clearly seen in all the human carotid arteries with advanced lesions in this study (see Fig. 4).

The elemental concentration information of human carotid arterial walls with advanced atherosclerotic lesions is presented in Table 2. Sample 1 refers to the normal carotid artery sample, samples 2, 3 and 4 are carotid arteries with advanced atherosclerotic lesion. Elemental information was extracted from the lesion and artery with this underlying lesion (labelled 'artery w lesion' in the table) separately. As expected, it is clearly seen that the phosphorus concentrations are elevated significantly with the calcification [19], the iron level is much higher in most of the advanced lesion areas and zinc levels are lower compared to the 'normal' carotid artery sample except sample 3, which shows much higher iron content in arterial wall than that in the adjacent lesion area. This may suggest that high iron content of the arterial wall could be one of the reasons for the development of atherosclerotic lesions. Again, these findings are consistent with our previous rabbit atherosclerosis studies [5,20]. This may suggest that the rabbit and/or $apoE^{-/-}$ transgenic mice are valid models for the atherosclerosis development in humans, and that research in these models may be suitable for human disease studies. High resolution work will be carried out to probe into the calcified clusters of human carotid arteries and atherosclerotic lesions in the future.

4.2. Mapping strontium (Sr) distribution in bone samples using Nuclear Microscopy

Strontium is an element that possesses similar chemical properties as calcium. Both exist as divalent cations in biological fluids which allow them to share the same pathways of absorption, homeostasis and excretion in the human body. Strontium is currently being used as the pharmacologically active component of osteoporosis drugs [21]. Excessive calcium intake has been associated with the arterial calcification mentioned above [22], it is possible that strontium will follow a similar mechanism (strontification).

The processes and mechanisms through which strontium acts on bones are only partially understood [22,23]. Major questions

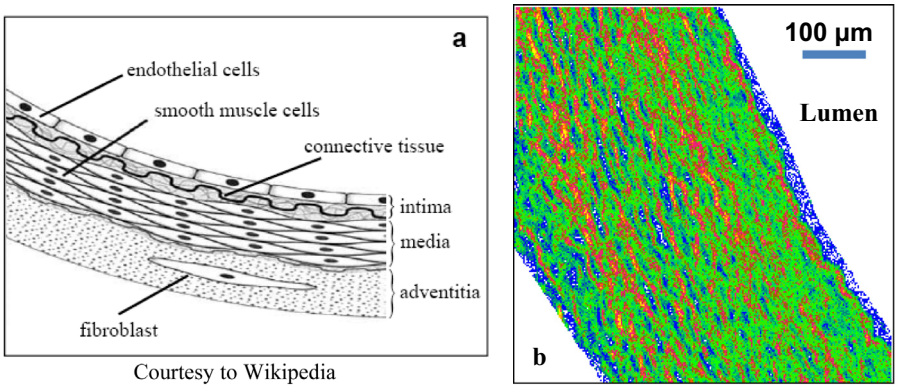

Fig. 2. a: Schematic representation of healthy arterial wall, b: Scanning Transmission Ion Microscopy image of healthy arterial wall.

Table 1
Elemental concentration in ppm by weight and statistical errors of intima, media and adventitia.

	P	S	Cl	Ca	K	Fe	Zn
Intima	**934** (84)	**2654** (111)	**16800** (151)	**847** (30)	**115** (25)	**9** (4)	**111** (14)
Media	**538** (63)	**2037** (88)	**15765** (110)	**982** (24)	**86** (21)	**22** (4)	**48** (8)
Advantitia	**640** (103)	**2575** (142)	**17242** (190)	**724** (38)	**166** (30)	**76** (10)	**39** (13)

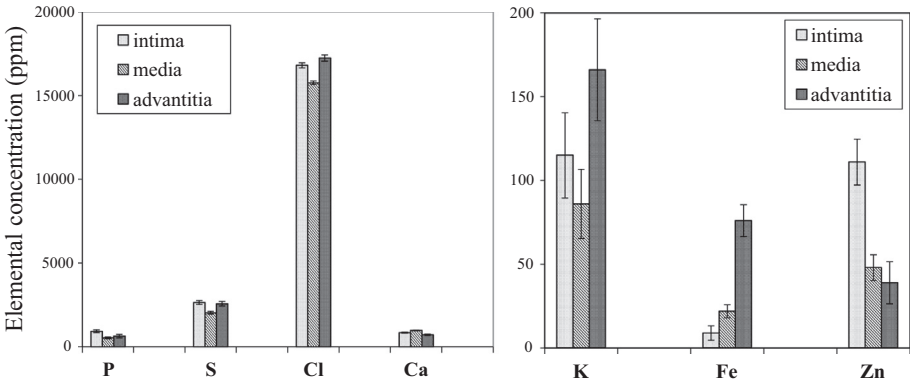

Fig. 3. Elemental concentration profile of arterial areas: intima, media and adventitia.

remaining to be answered are related to the incorporation of Sr into the bone matrix, its spatial distribution and the extent to which Sr can replace Ca in the bone matrix. These questions are currently being addressed in a research project involving long-term supplementation of Sr in rat diet. Using the NM beamline, we have taken elemental maps of the Sr distribution and concentration of rat bone samples.

For NM analysis of rat bone, the proximal femur was dissected and embedded in epoxy resin (EpoFix Kit, Struers Inc., OH, USA). The embedded femur was cut under constant water irrigation along the coronal plane with a low speed (<150 rpm) diamond saw (Isomet, Buehler, IL, USA) to avoid sample heating and tissue damage. The cross-section was then ground and polished (TegraPol-11, Struers Inc.) to prepare the surface for NM analysis.

Polished bone sections of about 2 mm thickness, which can be highly insulating sample material, were coated with a thin layer of carbon to avoid charging under the proton beam. Charging often occurs when non-conducting samples are irradiated by proton beams, because charge accumulation can lead to large localised electric fields. These fields in turn can lead to energetic electrons which give rise to electron bremsstrahlung and therefore background noise in the X-ray spectra. It is known that a carbon coating can minimize this charge accumulation in some samples. Fig. 5 shows the X-ray spectra of rat bone samples with and without carbon coating, indicating that in our case there is a significant reduction in background.

Bone sections of 2 mm thickness are considered thick targets for a 2.1 MeV proton beam, since protons do not penetrate through the sample. The STIM technique is therefore not applicable for fast sample positioning: Therefore the initial sample positioning was based on RBS carbon maps. High statistics RBS and PIXE list-mode runs were then assembled for quantitative measurements. It is worth mentioning that a special filter was designed for detecting minute amounts of strontium in calcium rich bone samples. After consideration of the absorption coefficients, a filter of 50 µm aluminum and 250 µm Kapton (Freude, Singapore) was chosen, leading to a large 10^4 reduction of the calcium K X-ray yield but allowing 82% transmission of the strontium K X-rays. Using this filter, pulse pile up was avoided, and the region of the spectrum where the strontium peak is located exhibited almost zero background (see Fig. 5). Fig. 6a shows the superimposed PIXE spectra from the two regions indicated in the Sr PIXE map shown in Fig. 6b. A clear difference of the strontium level is readily observable both in the strontium distribution map (6b) and PIXE spectra (6a).

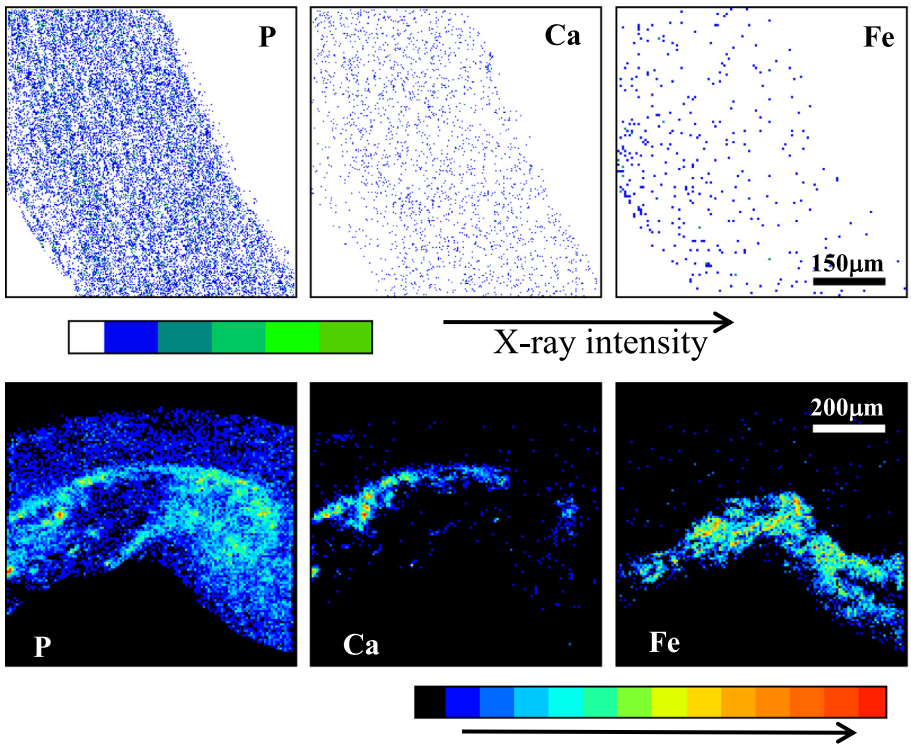

Fig. 4. Elemental distribution maps of human carotid artery normal control (top three images) and with advanced atherosclerotic lesion (bottom three images). The advanced atherosclerosis tissue show calcification and large clusters of iron deposits: Note the anti-correlation between calcium and iron of the artery with advanced lesion.

Table 2
Elemental concentration in ppm by weight and statistical errors of human carotid artery With/without advanced atherosclerotic lesions.

Sample		Scan size (μm)	P	S	Cl	K	Ca	Fe	Zn
1	Normal artery	200	**704** (84)	**2422** (114)	**16602** (150)	122 (31)	**851** (25)	**36** (6)	**66** (11)
2	Artery w lesion	2000	**4474** (72)	**2185** (70)	**4320** (69)	**633** (21)	**1432** (19)	**8** (2)	**11** (3)
	Lesion area		**5780** (52)	**2327** (47)	**4419** (44)	**350** (19)	**8030** (24)	**55** (2)	**21** (2)
3	Artery w lesion	1000	**1582** (55)	**2292** (66)	**4860** (73)	**850** (26)	**382** (16)	**464** (12)	**21** (5)
	Lesion area		**3678** (51)	**1510** (50)	**4260** (55)	**344** (28)	**5251** (32)	**96** (5)	**10** (3)
4	Artery w lesion	800	**552** (60)	**3620** (83)	**6462** (90)	**952** (31)	**870** (24)	**36** (6)	**46** (8)
	Lesion area		**1926** (23)	**1756** (26)	**4238** (30)	**557** (12)	**1820** (13)	**426** (5)	**17** (2)

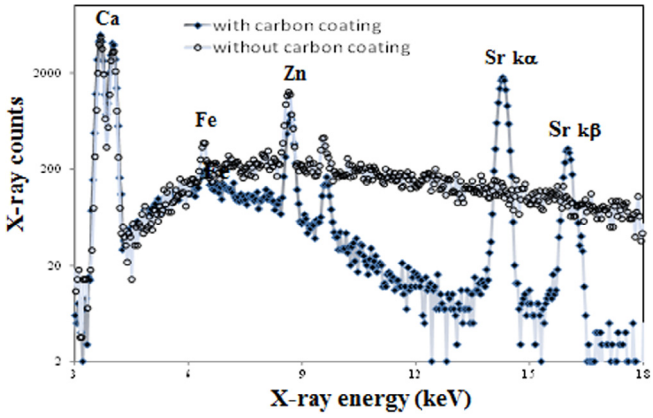

Fig. 5. PIXE spectra of bone sections showing the significantly reduced background in the carbon coated sample allowing more accurate detection of strontium. (2.1 MeV proton, filter: 50 μm Al + 250 μm Kapton).

The optimized setup for strontium analysis in bone described above has been applied to the strontium mapping and quantitative measurement of the proximal femur as shown in Fig. 7. As can be seen from the elemental maps shown in Fig. 7, at a beam spot size of about 1 μm, it is possible to associate calcium and strontium deposition with anatomical structures, namely the outer solid shell of bone (corticula) and its spongy interior (trabecular bone). While strontium was found distributed everywhere in the bone structure, the strontium concentration was found to be higher at the surface areas of the trabecula, i.e. the newly formed bone. For quantitative evaluation, for example, to compare strontium to calcium ratios, measurements can be either done at isolated spots or as a 'line scan' in which the width of the scanned area is reduced to assess changes in strontium deposition/incorporation relative to calcium (see Fig. 8). Strontium to calcium ratios in bone reveal to what extent calcium has been replaced in the bone matrix.

Line scan profiles of any part of the strontium and calcium images can be generated offline to show a more pronounced correlation between strontium and calcium as shown in Fig. 8.

As demonstrated above, the usefulness of the Nuclear Microscope beam line lies in its capability of elemental mapping at μg/g dry weight level at spatial resolutions of 1 μm and the ability to measure the concentrations of trace elements with high quantitative accuracy, independent of the chemical state of the element.

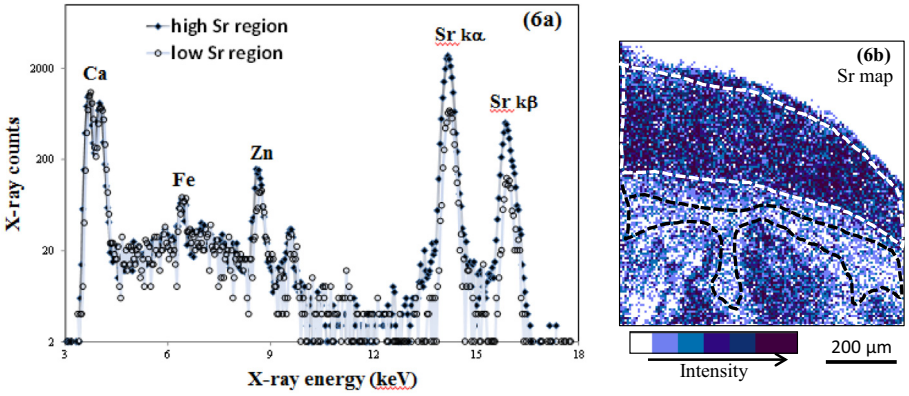

Fig. 6. PIXE spectra of different Sr concentration regions of rats' vertebra bone section, Sr map is shown on the right with high Sr region marked with white dotted line and low Sr region marked with black dotted line.

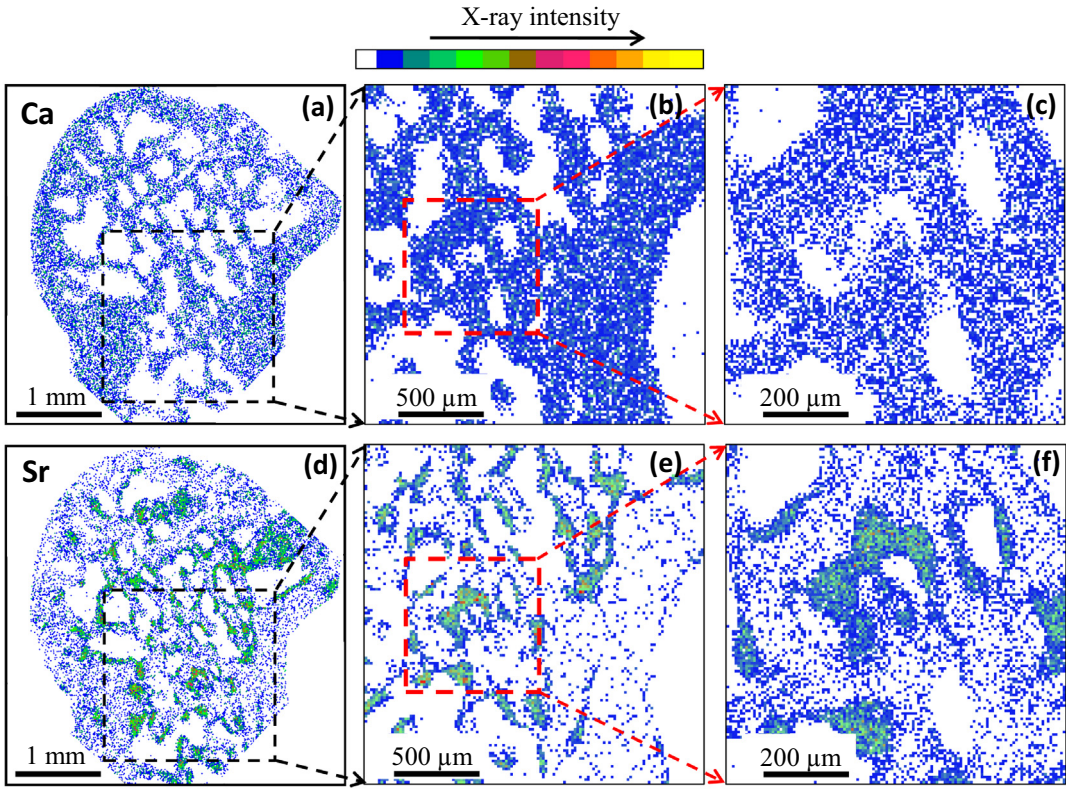

Fig. 7. Strontium and calcium distribution maps of bone samples at different magnifications (a,d: 4 mm scans, b,e: 2 mm scans, c,f: 800 μm scans).

Therefore, Nuclear Microscopy is ideally suited for imaging the morphology of tissues and mapping minute amount trace elements present in bone tissues.

5. Biomedical applications of single cell imaging beam line

It is well known that conventional light microscopy is limited to resolving features bigger than 250 nm due to the fundamental diffraction limits of visible light; and that electron microscopy, even though it can produce images with nanometer resolution, is limited to surface features because of the electron scattering properties and the short range of secondary electrons being emitted for the sample. Therefore a need arises to develop higher resolution probes to image chemical/biological changes at subcellular levels for research in many diseases, e.g. brain dopamine cell deficiency in Parkinson's disease; insulin resistance in diabetes and genetic changes in cancer.

The straight path characteristics of fast light MeV ion beams focused to sub 100 nm spot sizes has enabled a range of imaging modalities, potentially opening up superior imaging modes in certain applications. Typically, proton or helium ion beams are used in such experiments. Helium ions tend to give better contrast than protons in STIM measurements, where the energy loss is the measured quantity. This is readily explained because the stopping power of MeV alpha particles is approximately 10-fold higher than that of MeV protons. Furthermore, the lateral scattering of the ion

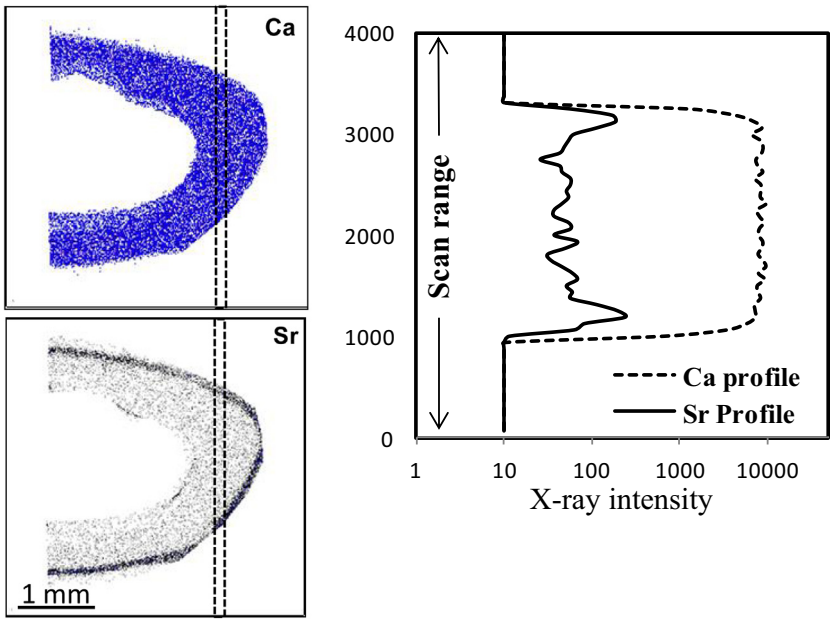

Fig. 8. Line profiles of the marked rectangular region on Ca and Sr maps (left) can be extracted.

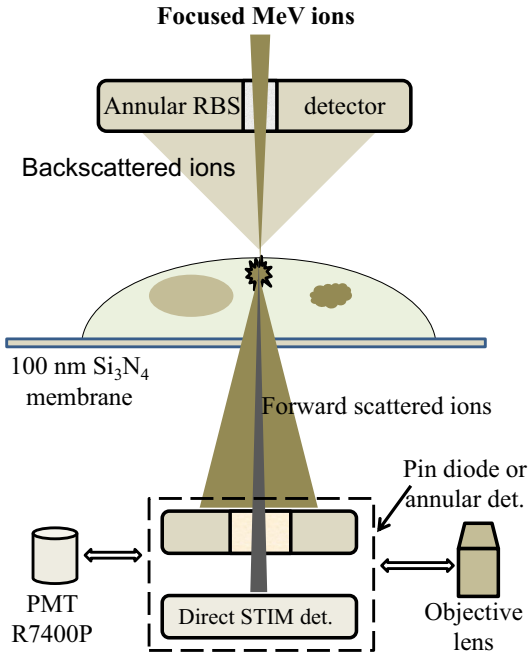

Fig. 9. Schematic setup of the CIBA Single Cell Imaging beamline. A focused ion beam interacts with a single cell on a 50 nm Si_3N_4 window. Simultaneously, backscattered (RBS), forward scattered (indirect STIM) and transmitted (direct STIM) ions are detected. A PMT, or an optical microscope may be swapped in for the STIM detector system, enabling target viewing and ion induced fluorescence measurements.

beam traversing the sample will clearly impact the resolution quality of STIM images. From calculations of ion trajectories, the lateral beam spread for 2 MeV protons after passing through a 1 μm thick cell is less than 10 nm, and for 1.5 MeV helium ions passing through a 1 μm thick cell, 93% of the ions are contained within 10 nm lateral range [24]. Therefore, for 50 nm spot sizes, beam broadening can essentially be considered minimal.

A schematic of the setup of the CIBA Single Cell Imaging beamline is shown in Fig. 9. This setup has enabled a novel mode of single cell imaging at the sub 50 nm level. The thickness of a dried whole cell is typically around 1–2 μm, and so the spatial resolution of the STIM image will not be degraded substantially by lateral scattering.

For such measurements, we have used well known cell preparation protocols, as well as in-house developed methods [8,25,26]. Basically cells are cultured on 50 nm or 100 nm thick silicon nitride windows in order to produce a monolayer of cells. In some cases the culture medium includes of nanoparticles (e.g. AuNPs) of specific concentrations. An example of a silicon nitride window chip is shown is Fig. 10. Each silicon nitride chip has a 3×5 array of 750×750 μm^2 windows. After the cell seeding, a vigorous sample preparation procedure is needed, including a cell wash with phosphate-buffered saline, a cell fix with glutaraldehyde, a complete dehydration process with different concentrations of ethanol, followed by critical-point drying. Typically several windows will break during the sample preparation procedures, therefore chips with more than 10 windows (in our case, 15) are recommended.

Helium ions are typically used for imaging, except for ion induced fluorescence measurements, where ion beam induced quenching of the optical emission is often seen. However, work is in progress in CIBA in order to develop probes that are resistant to helium ion quenching (see below – Fig. 12). As an early example of single cell STIM imaging, one of the cells shown in Fig. 10c was scanned using an 1.5 MeV alpha particle beam focused to 80 nm. The resulting images are shown in Fig. 11. Fig. 11a shows an on-axis STIM image of the cell, and shows the cell nucleus, nucleoli and smaller structures which are not observed in the corresponding SEM image (Fig. 11c); noting that SEM depicts the surface features only. Fig. 11b shows a higher magnification on-axis STIM image and Fig. 11d shows the SEM image of equivalent region. The nucleus and small structures are clearly shown in the STIM images. Some of these structures are also observed in the SEM images and are therefore surface features.

A further project carried out in CIBA is the study of the uptake of lanthanide-doped nanoparticles within single whole cancerous cells (HeLa). Direct STIM, FSTIM and AIF (alpha particle induced

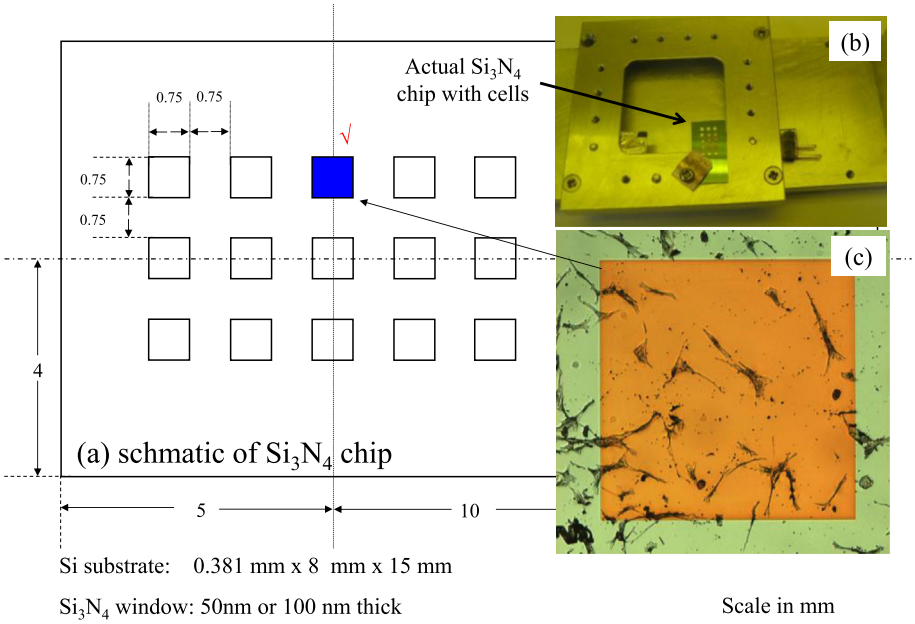

Fig. 10. (a) schematic diagram of silicon nitride chip having 3 × 5 arrays of 50 nm or 100 nm thick SiN window of 750 × 750 μm^2 (b) chip with single cell ready for imaging; (c) optical micrograph of one of the Si_3N_4 windows with individual cells.

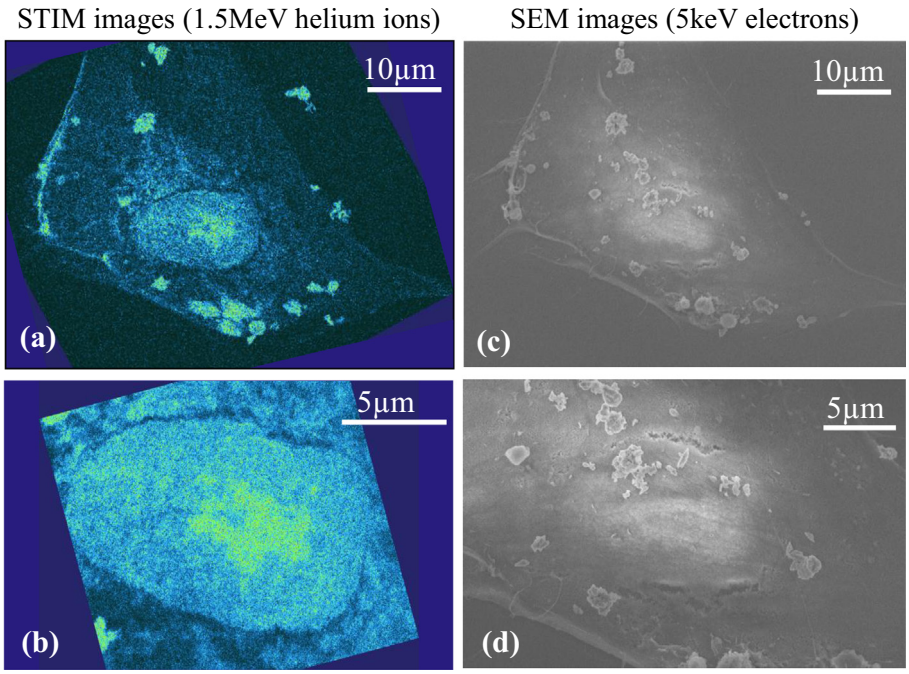

Fig. 11. (a) on-axis STIM (direct STIM) image of a cell indicating the nucleus, nucleoli and various structures not observed in the SEM image (c), (b) is a higher magnification on-axis STIM image of the same cell, showing the central region of the cell and the nucleus, with smaller features inside the nucleus. The equivalent SEM image (d) shows only the surface features of the cell (the surface clusters were assumed to be accumulated osmium tetroxide on the surface introduced during the cell preparation protocol).

fluorescence) have been used to image the single cells prepared on 100 nm thick silicon nitride windows [26]. These images are shown in Fig. 12.

The STIM image displays the energy loss variation of the 1.6 MeV alpha particles as they pass through the cell, and this clearly reveals structural information of the Hela cell. The alpha particle-induced fluorescence (AIF) images depict the fluorescent nanoparticles within the cell. As can be observed, the individual nanoparticles and clusters are resolved clearly in the alpha particle induced fluorescence images, and it is worth noting that this spatial resolution is much better than the corresponding optical fluorescence image shown in Fig. 13.)

The imaging of nanoparticles with high Z can be improved if off-axis alpha STIM is used. Off-axis STIM is a technique based on the detection of forward scattered ions, the energy of the transmitted ions scattered at a slight angle (~10°) is measured [27]. This technique is therefore governed by the well-known Rutherford scattering formula:

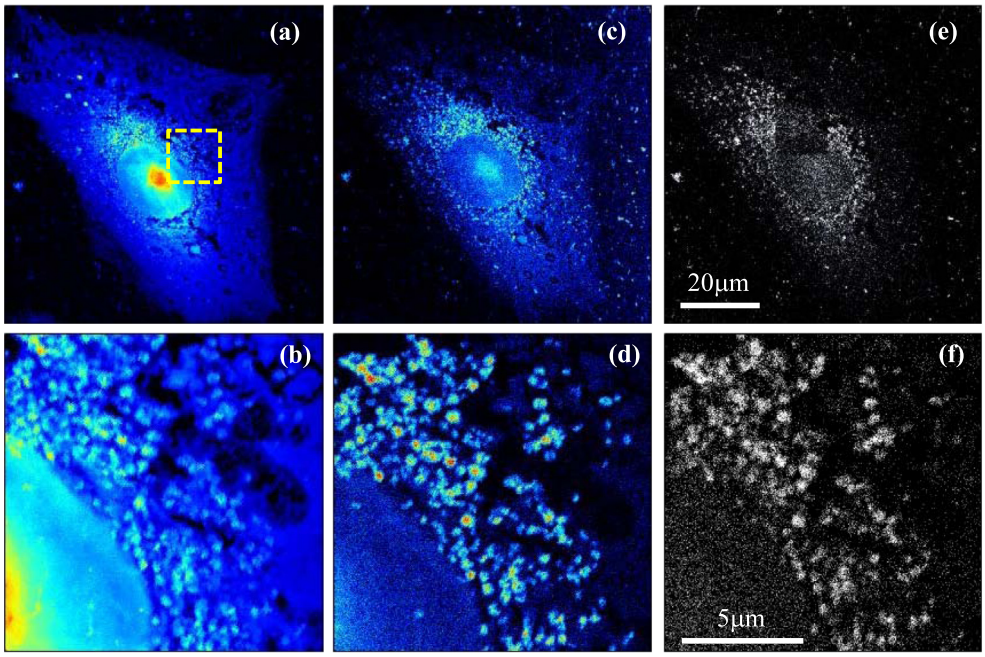

Fig. 12. The images in the top row (12a,c, and e) are STIM, FSTIM and AIF images of a HeLa cell using a 1.6 MeV alpha particle beam with a scan size of 90 μm. The images in the bottom row (12b,d, and f) are high resolution STIM, FSTIM and AIF images of a region of interest (depicted by the yellow square in 12a) from the same HeLa cell with a scan size of 13 μm. A median fit was used in each case, using 15 alpha particle counts per pixel (pixel normalization). Figures (a,b) are STIM images of rhe cell, showing structural details within the cell. Figures (c,d) are off-axis STIM images indicating high contrast for the lanthanide-doped nanoparticles; Figures (e.f) are AIF images: Note that there is some helium bleaching in Fig. 13e. This image was taken after the high resolution AIF image shown in 12f, which took 1 h to accumulate. (For interpretation of the references to colour in this figure legend, the reader is referred to the web version of this article.)

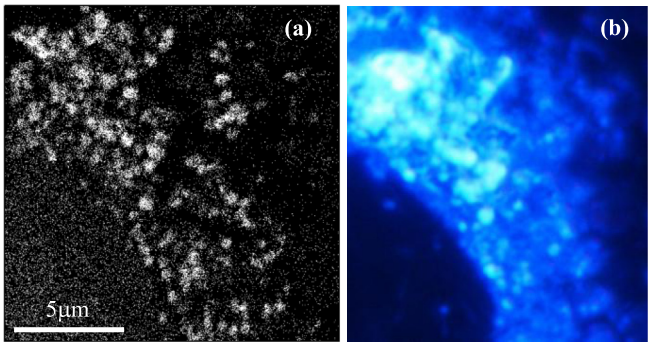

Fig. 13. (a) AIF image (b) 980 nm laser induced fluorescence image

$$\frac{d\sigma}{d\Omega} = \frac{Z_1^2 Z_2^2 e^4}{16 E_0^2 Sin^4\left(\frac{\theta}{2}\right)}$$

where σ is the Rutherford cross section, Ω is the detector solid angle, Z_1 is the atomic number of the incoming ion, and Z_2 is the atomic number of the target atom, E_0 is the incoming ion energy, and θ is the scattering angle.

Nanoparticles made of lanthanide or gold have relatively large Z, therefore imaging them via forward STIM will result in images with larger contrast than direct STIM can achieve. Therefore a combination of on-axis STIM, to highlight the internal cell features, and off-axis STIM to image high Z nanoparticles, has advantages in imaging nanoparticles within single whole cells.

6. Conclusion

We have shown that state-of-the-art Nuclear Microscopy is a versatile and quantitative analytical technique, and that the single cell analysis by light ion nano-beams is a promising technique for sub cellular imaging. The facilities available at CIBA are tools for the advanced microscopy of biological tissues and single whole cells and continuous efforts are being made to explore this exciting field.

References

[1] D. Mous, R. Haitsma, T. Butz, R.-H. Flagmeyer, D. Lehmann, J. Vogt, Nucl. Instr. Meth. Phys. Res. Sect. B 130 (1997) 31–36.
[2] F. Watt, I. Orlic, K.K. Loh, C.H. Sow, P. Thong, S.C. Liew, T. Osipowicz, T.F. Choo, S.M. Tang, Nucl. Instr. Methods B85 (1994) 708.
[3] F. Watt, J.A. van Kan, I. Rajta, A.A. Bettiol, T.F. Choo, M.B.H. Breese, T. Osipowicz, Nucl. Instr. Methods B 210 (2003) 14–20.
[4] F. Watt, Xiao Chen, Armin Baysic De Vera, C.N. Udalagama, Ren Minqin, J.A. van Kan, A.A. Bettiol, The Singapore high resolution single cell imaging facility, Nucl. Instr. Meth. Phys. Res. B 269 (2011) 2168–2174.
[5] M.Q. Ren, F. Watt, B.K.H. Tan, B. Halliwell, Free Radical Biol. Med. 34 (6) (2003) 746.
[6] G.W. Grime, M. Dawson, M. Marsh, I.C. McArthur, F. Watt, Nucl. Instr. Meth. B54 (1991) 52 (latest version on www.microbeams.co.uk/downloads).
[7] J.F. Ziegler, The Stopping and Range of Ions in Matter, vol. 2–6 (Pergamon Press, 1977–1985), http://www.srim.org/.
[8] X. Chen, C.B. Chen, C. Udalagama, M.Q. Ren, K.E. Fong Ee, L. Yung, G. Pastoria, A. A. Bettiol, F. Watt, Bio-Physical J. 104 (7) (2013) 1419.
[9] G.W. Grime, F. Watt, Beam Optics of Quadrupole Probe Forming Systems, Adam Hilger, Bristol, 1984, p. 63.
[10] J.A. van Kan, P. Malar, Armin Baysic de Vera, Rev. Sci. Instrum. 83 (2012) 02B902.
[11] F. Zhang, J.A. van Kan, S.Y. Chiam, F. Watt, Nucl. Instr. Methods B 260 (2007) 474.
[12] A.A. Bettiol, C. Udalagama, F. Watt, Nucl. Instr. Methods B 267 (2009) 2069.
[13] F. Watt, X. Chen, C. Chen, C. Udalagama, M. Ren, G. Pastorin, A. Bettiol, Cosmos 9 (2013) 1–10.
[14] M.Q. Ren, W.Y. Ong, X.S. Wang, F. Watt, Exp. Neurol. 184 (2003) 947.
[15] M.Q. Ren, R. Rajendran, P. Ning, B.K.H. Tan, C.N. Ong, F. Watt, A. Jenner, B. Halliwell, Free Radical Biol. Med. 41 (2006) 222–225.
[16] M.Q. Ren, E. Huang, B. Konstanze, R. Rajendran, B.J. Wu, B. Halliwell, F. Watt, R. Stocker, Nucl. Instr. Methods B 260 (2007) 240.
[17] M. Mayer, SIMNRA User's Guide, Report IPP 9/113, Max-Planck-Institut für Plasmaphysik, Garching, Germany, 1997.
[18] J.L. Campbell, T.L. Hopman, Nucl. Instr. Methods B170 (2000) 193.
[19] R. Rajendran, M.Q. Ren, J.A. Ronald, B.K. Rutt, B. Halliwell, F. Watt, Free Radical Biol. Med. 53 (9) (2012) 1675.

[20] F. Watt, R. Rajendran, M.Q. Ren, B.K.H. Tan, B. Halliwell, Nucl. Instr. Methods B 249 (2006) 646.
[21] P. Ammann, I. Badoud, S. Barraud, R. Dayer, R. Rissoli, J. Bone Mine. Res. 22 (9) (2007) 1419.
[22] P.J. Marie, Mol. Interventions 10 (5) (2010) 305.
[23] E. Shorr, A.C. Carter, J. Clin. Endocrinol. Metab. 12 (1952) 928.
[24] X. Chen, C.N.B. Udalagama, C.B. Chen, A. Bettiol, D. Pickard, T. Venkatesan, F. Watt, Biophys. J. 101 (2011) 1788.
[25] M.Q. Ren, J.A. van Kan, A.A. Bettiol, D. Lim, Y.G. Chan, B.H. Bay, H.J. Whitlow, T. Osipowicz, F. Watt, Nucl. Instr. Methods B260 (2007) 124.
[26] Z.H. Mi, Y.H. Zhang, S.K. Vanga, C.B. Chen, H.Q. Tan, F. Watt, X.G. Liu, A.A. Bettiol, Nat. Commun. 6 (2015), Article number: 8832.
[27] A.A. Bettiol, Z.H. Mi, S.K. Vanga, C.B. Chen, Y. Tao, F. Watt, Nucl. Instr. Methods B348 (2015) 131.